Predicting Galaxy Star Formation Rates via the Co-evolution of Galaxies and Halos

Douglas F. Watson[1]⋆†, Andrew P. Hearin[1,2,3], Andreas A. Berlind[4], Matthew R. Becker[5,6,7], Peter S. Behroozi[8], Ramin A. Skibba[9], Reinabelle Reyes[1], Andrew R. Zentner[10,11], Frank C. van den Bosch[12]

[1] *Kavli Institute for Cosmological Physics, 5640 South Ellis Avenue, The University of Chicago, Chicago, IL*
[2] *Fermilab Center for Particle Astrophysics, Fermi National Accelerator Laboratory, Batavia, IL,*
[3] *Yale Center for Astronomy & Astrophysics, Yale University, New Haven, CT*
[4] *Department of Physics and Astronomy, Vanderbilt University, Nashville, TN*
[5] *SLAC National Accelerator Laboratory, Menlo Park, CA 94025*
[6] *Kavli Institute for Particle Astrophysics and Cosmology, Stanford, CA 94309, USA*
[7] *Department of Physics, School of Humanities and Sciences, Stanford University, Stanford, CA 94309, USA*
[8] *Space Telescope Science Institute, 3700 San Martin Drive, Baltimore, MD 21218*
[9] *Department of Physics, Center for Astrophysics and Space Sciences, University of California, 9500 Gilman Dr., La Jolla, San Diego, CA 92093*
[10] *Department of Physics and Astronomy, University of Pittsburgh, Pittsburgh, PA 15260*
[11] *Pittsburgh Particle physics, Astrophysics and Cosmology Center (PITT PACC)*
[12] *Department of Astronomy, Yale University, P.O. Box 208101, New Haven, CT*

8 October 2014

ABSTRACT

In this paper, we test the *age matching* hypothesis that the star formation rate (SFR) of a galaxy of fixed stellar mass is determined by its dark matter halo formation history, and as such, that more quiescent galaxies reside in older halos. This simple model has been remarkably successful at predicting color-based galaxy statistics at low redshift as measured in the Sloan Digital Sky Survey (SDSS). To further test this method with observations, we present new SDSS measurements of the galaxy two-point correlation function and galaxy-galaxy lensing as a function of stellar mass and SFR, separated into quenched and star-forming galaxy samples. We find that our age matching model is in excellent agreement with these new measurements. We also employ a galaxy group finder and show that our model is able to predict: (1) the relative SFRs of central and satellite galaxies, (2) the SFR-dependence of the radial distribution of satellite galaxy populations within galaxy groups, rich groups, and clusters and their surrounding larger scale environments, and (3) the interesting feature that the satellite quenched fraction as a function of projected radial distance from the central galaxy exhibits an $\sim r^{-.15}$ slope, independent of environment. The accurate prediction for the spatial distribution of satellites is intriguing given the fact that we do not explicitly model satellite-specific processes after infall, and that in our model the virial radius does not mark a special transition region in the evolution of a satellite, contrary to most galaxy evolution models. The success of the model suggests that present-day galaxy SFR is strongly correlated with halo mass assembly history.

Key words: cosmology: theory — dark matter — galaxies: haloes — galaxies: evolution — galaxies: clustering — galaxies: star formation

1 INTRODUCTION

One of the principal goals of galaxy evolution theory is to understand the connection between the properties of galaxies and their host dark matter halos. There is now

⋆ NSF Astronomy & Astrophysics Postdoctoral Fellow
† email: dfwatson@kicp.uchicago.edu

a well-established relation between the stellar mass of a galaxy and the mass of the halo in which it resides (e.g., Yang et al. 2012; Leitner 2012; Wang et al. 2012; Moster et al. 2013; Behroozi et al. 2013a; Kravtsov 2013; Kravtsov et al. 2014). Moreover, the fact that the stellar mass-to-halo mass connection remains tight across cosmic time (Conroy & Wechsler 2009; Behroozi et al. 2013b; Watson & Conroy 2013; Lu et al. 2014) suggests that there are likely further links between halo properties and the star formation rate (SFR) of galaxies. With this as motivation, the aim of the present work is to address the following question: is there a simple link between the SFR of galaxies and the dark side of the universe?

The complex nature of star formation in galaxies indicates that the relationship between the SFR of a galaxy and the properties of its host dark matter halo may be complicated. First, at *fixed luminosity* or *fixed stellar mass*, there exists a clear bimodality in the distribution of galaxy color/SFR, with distinct red/quenched and blue/star-forming populations (Blanton et al. 2003; Baldry et al. 2004; Bell et al. 2004; Blanton et al. 2005; Cooper et al. 2006; Wyder et al. 2007; Wetzel et al. 2012; Cooper et al. 2012). Additionally, galaxy color/SFR depends on environment: denser environments, such as rich groups and clusters, are populated by significantly more red sequence galaxies than actively star-forming ones (Balogh et al. 1999; Blanton et al. 2005; Weinmann et al. 2006, 2009; Peng et al. 2010, 2012; Carollo et al. 2013; Tal et al. 2014). Furthermore, the specific processes that attenuate SFR in a 'central' galaxy (the galaxy at the minimum of the halo potential well) may be distinct from those governing the 'satellite' galaxies orbiting the central (van den Bosch et al. 2008). Finally, the SFR/color dependence of galaxy location within the cosmic web also manifests in measurements of two-point statistics; as a function luminosity or stellar mass, red/quenched galaxies exhibit stronger clustering than blue/star forming galaxies (e.g., Norberg et al. 2002; Zehavi et al. 2002, 2005; Li et al. 2006; Zehavi et al. 2011; Yang et al. 2012; Mostek et al. 2013; Guo et al. 2014a). Such observed complexities may lead one to conclude that complicated modeling of the physics governing the quenching of galaxies is required to reproduce observed galaxy statistics.

However, in a pair of recent papers introducing the *age matching* formalism (Hearin & Watson 2013; Hearin et al. 2014, hereafter Papers I & II, respectively), it was shown that in fact a very simple model for galaxy color can account for the rich variety of trends exhibited by galaxies in the low-redshift universe. The central hypothesis of age matching is that at fixed luminosity (or fixed stellar mass), galaxy color is in monotonic correspondence with a proxy for halo age, at fixed halo maximum circular velocity V_{max}. In Paper I, this prescription was shown to accurately reproduce the observed $g - r$ color-dependent clustering of galaxies in the Sloan Digital Sky Survey (SDSS: York et al. 2000) for the luminosity-selected galaxy samples presented in Zehavi et al. (2011), as well as the scaling between $g - r$ color and host halo mass. In Paper II, similar success of the age matching formalism was demonstrated for model predictions of new measurements of both SDSS clustering and galaxy-galaxy lensing as a function of stellar mass and $g - r$ color.

However, $g - r$ color and star formation activity are not perfectly correlated. For instance, galaxies that are actively forming stars can often appear red due to the ubiquitous presence of dust (e.g., Stein & Soifer 1983; Maller et al. 2009; Masters et al. 2010). Furthermore, $g - r$ color is the convolution of many physical properties of galaxies, including: stellar age, metallicity, and instantaneous SFR. Thus, a model for the color-dependence of galaxy location within the cosmic web may not smoothly translate to a model for the SFR dependence. In the present study, we demonstrate how age matching, without modification to the technique introduced in Papers I & II, is equally successful at reproducing new SDSS measurements of stellar mass- and SFR-dependent clustering and galaxy-galaxy lensing. As we will demonstrate in a forthcoming paper (Watson, Skibba & Hearin 2014, in prep) studying *marked* correlation functions (Skibba et al. 2006, 2013), this simultaneous success of our model is primarily due to the surprising observational fact that the two-point function is almost entirely insensitive to the choice of SFR or $g - r$ as a star formation indicator.

Additionally, in this paper we take a sharp focus on the population of satellite galaxies. While satellites are in the minority by number, the physics governing satellite galaxy SFR is a key ingredient to painting a complete picture of the theory of galaxy evolution. Satellite galaxies can be subject to a number of complex processes which are believed to stifle their star formation as they orbit within the gravitational potential well of their host halo. These include the removal of cold gas from the disc due to ram pressure (Gunn & Gott 1972), the stripping of the surrounding hot gas reservoir, known as 'strangulation' (Larson et al. 1980), disruption of satellite galaxies due to tidal stripping (Purcell et al. 2007; Watson et al. 2012), and 'harassment' by gravitational interactions with other nearby galaxies (Moore et al. 1998).

In age matching there is *no* explicit modeling of such post-accretion processes. And yet, we will demonstrate that this remarkably simple model accurately predicts the radial profiles of star-forming and quenched satellite galaxies within and around the environment of groups, rich groups, and clusters. As discussed in § 5, the success of age matching at reproducing these trends indicates that in much of the literature on satellite evolution, the influence of post-accretion processes on quenching satellites has been over-estimated.

The paper is laid out as follows. In § 2 we describe the data, simulation and halo catalogs incorporated throughout this work. An overview of the age matching and the more generic "conditional abundance matching" formalism is given in § 3. In § 4 we present our main results. Specifically, in § 4.1 we show our model predictions for new measurements of the SFR-dependent two-point correlation function and galaxy-galaxy lensing signal. In § 4.2 we study the spatial properties of star-forming and quenched satellite galaxies within and around halos. In § 5 we provide a discussion and interpretation of our findings. We conclude in § 6 with a brief summary of our primary results. Throughout this work we assume a flat ΛCDM cosmological model with $\Omega_m = 0.27$ and Hubble constant $H_0 = 70$ km s^{-1} Mpc^{-1}.
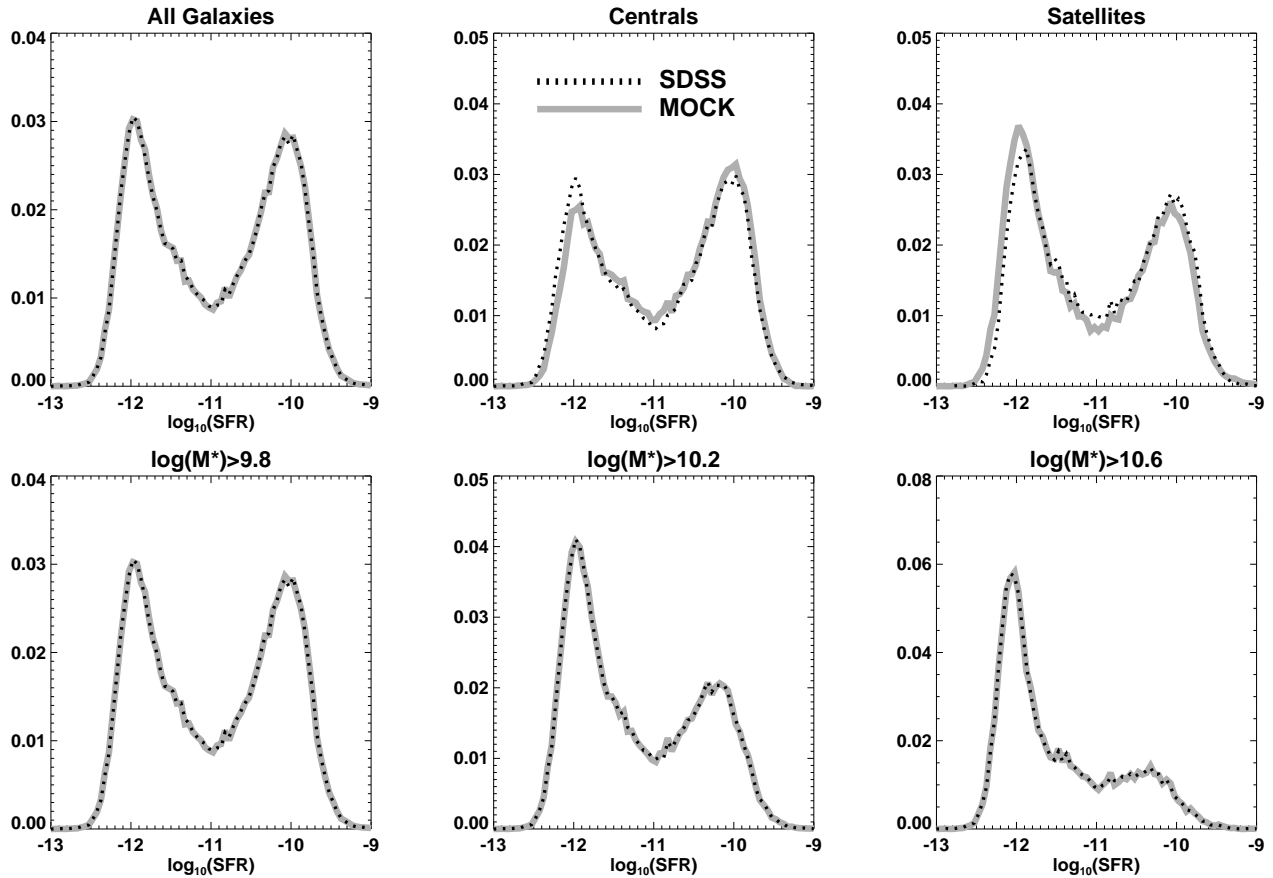
Figure 1. The probability distribution functions (PDFs) of the specific star formation rate (sSFR) of galaxies in our mock catalog (gray solid curves) as compared to those measured in the SDSS galaxy catalogs (dotted black curves). By construction, the PDFs of sSFR of our mock galaxies are in exact agreement with the data for all the galaxies in our sample (top left panel) as well as three stellar mass threshold samples (bottom row): $\log_{10}(M_*) > [9.8, 10.2, 10.6]$. Since our sSFR assignment to mock galaxies is blind to the distinction between central and satellite galaxies, the resultant PDFs in the center and right panels of the top row are *predictions* of age matching, and demonstrate a non-trivial success of the technique.

2 CATALOGS AND MEASUREMENTS

As our baseline galaxy sample and halo catalogs are identical to those used in Papers I & II, we only briefly sketch the essential elements of these catalogs here, and refer the reader to Papers I & II for further details.

For our galaxy data, we use a volume-limited galaxy sample from DR7 of the Sloan Digital Sky Survey (York et al. 2000; Abazajian et al. 2009), spanning the redshift range $0.02 < z < 0.067$, and complete to $\log_{10} M_*/M_\odot > 9.8$. We have identified galaxy groups in this sample using the friends-of-friends algorithm presented in Berlind et al. (2006); for brevity, we refer to this sample as our $M_*^{9.8}$ SDSS group catalog.

We have cross-matched the $M_*^{9.8}$ catalog with the specific star formation rate (sSFR) measurements taken from the MPA-JHU catalog, publicly available at http://www.mpa-garching.mpg.de/SDSS/DR7. The measurements are based on the Brinchmann et al. (2004) spectral reductions that utilize the strength of Hα emission to estimate present-day star formation activity, along with updated prescriptions for fiber aperture corrections and ac-

tive galactic nuclei (AGN) as detailed in Salim et al. (2007). Specifically, sSFRs are primarily derived from emission lines (mostly Hα), but in the cases of strong AGN contamination or no measurable emission lines, the sSFRs are inferred from Dn4000 in the galaxy spectrum (Kauffmann et al. 2003).

Our mock catalog is constructed from halos and subhalos in the Bolshoi N−body simulation (Klypin et al. 2011), based on publicly available ROCKSTAR merger trees and halo catalogs (Behroozi et al. 2013a,b)[1]. The simulation has a volume of $250^3\,h^{-3}\mathrm{Mpc}^3$ with 2048^3 dark matter particles of mass $1.9 \times 10^8 h^{-1} M_\odot$, and a cold dark matter (ΛCDM) cosmological model with $\Omega_\mathrm{m} = 0.27$, $\Omega_\Lambda = 0.73$, $\Omega_\mathrm{b} = 0.042$, $h = 0.7$, $\sigma_8 = 0.82$. For details on the Bolshoi database, see Riebe et al. (2013).

From the $M_*^{9.8}$ galaxy sample, we present new measurements of the two-point projected correlation function (2PCF), and the galaxy–galaxy lensing signal ($\Delta\Sigma$), as a function of stellar mass and SFR. Specifically, we di-

---

[1] ROCKSTAR halo catalogs and merger trees are publicly available at http://hipacc.ucsc.edu/Bolshoi/MergerTrees.html

vide the galaxies into 'star-forming' and 'quenched' populations by making a cut on the measured value of sSFR at $10^{-11}\mathrm{yr}^{-1}$. The clustering and lensing measurements are performed both observationally and in the simulation in the same manner as described in detail in Paper II. We make our mock galaxy catalog publicly available at http://logrus.uchicago.edu/~aphearin.

In order to investigate satellite-specific properties of quenched and star-forming galaxies addressed in § 4.2 we rely on our galaxy group finder to designate central and satellite galaxies in both the mock and the SDSS data. Specifically in each identified SDSS group, we label the galaxy with the highest stellar mass as a central and all remaining galaxies in the group as satellites. In our mock catalog, we follow the exact same procedure. By reproducing the same procedure in both SDSS data and mocks, we can compare the two without concern for group finding errors in the central/satellite assignment.

3   METHODOLOGY

Our main approach is to assign stellar masses and SFRs of galaxies to (sub)halos within the Conditional Abundance Matching (CAM) formalism (as fully detailed in § 4.3 Paper II). This formalism begins by using the abundance matching technique (e.g., Kravtsov et al. 2004; Vale & Ostriker 2004; Tasitsiomi et al. 2004; Vale & Ostriker 2006; Trujillo-Gomez et al. 2011; Rodríguez-Puebla et al. 2012; Watson et al. 2012; Hearin et al. 2013; Reddick et al. 2013; Kravtsov et al. 2014) to assign stellar masses to halos and subhalos in Bolshoi to create a volume-limited SDSS mock galaxy catalog. In particular, we abundance match the exact stellar mass function of our galaxy sample against the (sub)halo property V_{peak}, (the highest circular velocity a halo has had over its entire merger history) using ~ 0.15 dex of scatter in M_* at fixed V_{peak}, using the algorithm developed in Hearin et al. (2013).[2] Thus as a result of this first phase of implementation of the CAM technique, our model naturally inherits the well known successes of traditional abundance matching which has been shown to reproduce a variety of observations including galaxy 2PCFs (Conroy et al. 2006; Reddick et al. 2013), close pair counts (Berrier et al. 2006; Berrier & Cooke 2012), $M_* - M_h$ relations (Conroy & Wechsler 2009; Wang & Jing 2010; Guo et al. 2010; Reddick et al. 2013), and group multiplicity functions (Hearin et al. 2013). We note that Kravtsov et al. (2014) recently demonstrated that improved photometric techniques used to measure stellar mass (Bernardi et al. 2013) lead to quite a significant effect on the stellar mass-to-halo mass relation predicted

by abundance matching, particularly for central galaxies of halos at the high-mass end ($M_{\mathrm{halo}} \gtrsim 10^{14} h^{-1} M_{\odot}$). We intend to explore the influence of this systematic in future work, when we comprehensively explore the age matching parameter space.

Once stellar masses have been assigned to our mock galaxies, we then proceed to model galaxy SFRs using CAM, a general formalism to study correlations at fixed mass between *any* galaxy property and *any* halo property. The fundamental quantity in CAM is $P(M_*, X_{\mathrm{gal}}|V_{\mathrm{max}}, X_{\mathrm{halo}})$, the probability that a galaxy of a given stellar mass M_* and galaxy property X_{gal} resides in a halo with circular velocity V_{max} and an additional halo property X_{halo}. We choose the same specific implementation of CAM known as *age matching*, introduced in Paper I and extended in Paper II. In age matching, the quantity X_{gal} is either $g - r$ color or sSFR, and X_{halo} is the halo property z_{starve}, which is characterized by certain epochs in a halo's mass accretion history (MAH) presumed to be linked to the starvation of the cold gas supply needed to continue fueling star formation. These epochs include: the redshift a halo (1) accretes onto a larger halo, (2) transitions from the fast- to slow-accretion regimes (halo formation redshift z_{form} for which we use the concentration-based approximation introduced in Wechsler et al. 2002 and explain in detail in Appendix A of Paper I), and (3) reaches a virial mass scale of $10^{12} h^{-1} M_{\odot}$. Paper II demonstrated that (1) and (2) are highly correlated, thus disregarding halo accretion has proven to yield equally good model predictions. Epoch (3) was introduced because the halo mass $10^{12} h^{-1} M_{\odot}$ demarcates a characteristic mass scale above which star formation is believed to become rapidly inefficient due to AGN feedback (Shankar et al. 2006; Teyssier et al. 2011; Martizzi et al. 2012), and to a lesser extent due to pressure-supported shocks that can heat infalling gas to the virial temperature (Dekel & Birnboim 2006). A halo is assigned a z_{starve} value based on whichever of these three epochs occurs first in its MAH[3], formally written as $z_{\mathrm{starve}} \equiv \mathrm{Max}\{z_{\mathrm{acc}}, z_{\mathrm{char}}, z_{\mathrm{form}}\}$.

However, one may wonder whether correlating galaxy sSFR with z_{starve} is necessary at all in the construction of a successful model. This is due to the following chain of logic: (1) more massive halos host galaxies of greater stellar mass, (2) the quenched fraction increases with stellar mass, and therefore, (3) quenched samples in a mock catalog constructed by drawing random sSFRs without any z_{starve} ranking will preferentially weight higher mass halos. These higher mass halos have earlier assembly times (at fixed stellar mass), and this so-called "assembly bias" has been shown to affect the clustering of halos (e.g., Wechsler et al. 2002). We have performed such a test (in Papers I & II as well) and have found that this effect alone is *far* too weak to yield a working model. This class of models that randomly draws sSFRs from the data without any rank-ordering predicts minimal difference in the clustering between the quenched and star-forming populations, indicating that the effect of halo assembly bias alone is not a strong enough mechanism to yield a significant enough split in the clustering (see

---

[2] Although it has recently been shown that V_{peak} is typically set during a major merger and therefore unlikely to be truly correlated with present day stellar mass in detail (Behroozi et al. 2013), the focus of the present paper is on predicting present day SFR, and so we consider refining the traditional abundance matching algorithm beyond our scope. However, we note that basing the stellar mass assignment on V_{acc} (the maximum circular velocity of a halo when it accretes onto a larger halo, thus becoming a subhalo) rather than V_{peak} has a negligible impact on the SFR predictions of the model.

[3] For details on calculating z_{starve} from halo merger trees, see the appendix of Paper I.

Zentner, Hearin & van den Bosch 2014 for a more comprehensive discussion).

In this paper, mock galaxies are assigned SFRs in the same manner as they are assigned $g - r$ colors in Paper II: for a given fixed stellar mass bin, sSFR values are drawn directly from the probability distribution function exhibited by our galaxy catalog, $P_{\rm SDSS}({\rm sSFR}|M_*)$. The collection of halos and subhalos in the corresponding stellar mass bin are then rank-ordered by $z_{\rm starve}$, such that the most quenched galaxy will be assigned to the halo with the largest $z_{\rm starve}$ value, and so forth. As seen in Fig. 5 of Paper II the halo formation epoch $z_{\rm form}$ (and hence, halo age) dominates the contribution to $z_{\rm starve}$ over most of the stellar mass range probed by our sample. We choose to not adopt a simpler model (i.e., $z_{\rm starve} = z_{\rm form}$) for consistency in this trilogy of papers and we reserve any model simplification/fine-tuning for future papers when we consider additional statistics (e.g., galactic conformity) and push to other stellar mass and redshift regimes. In the end, age matching simply posits that *quenched galaxies reside in old halos*, though the more general CAM formalism allows for the exploration of any galaxy-halo property correlation.

The above procedure results in a mock galaxy catalog whose sSFR distribution is, by construction, in exact agreement with $P_{\rm SDSS}({\rm sSFR}|M_*)$. This agreement is illustrated by the probability distribution functions (PDFs) in the top left and bottom panels of Fig. 1. We emphasize that the purpose of the rank-ordering is to introduce, at fixed stellar mass, a correlation between galaxy SFR and $z_{\rm starve}$. However, as was the case for color in Papers I & II, our technique only uses the property $z_{\rm starve}$ and $P_{\rm SDSS}({\rm sSFR}|M_*)$ to assign SFRs to the mock galaxies, but does *not* distinguish between central and satellite galaxies in the SFR assignment. In fact, in age matching central and satellite galaxies of the same stellar mass have different SFR distributions strictly due to differences in the assembly histories of host halos and subhalos. Therefore, there is no guarantee that our PDFs will be correctly predicted for the sub-populations of centrals and satellite. Nonetheless, as can be seen in the top middle and right panels of Fig. 1, age matching does indeed successfully predict central and satellite SFRs. We return to this point in § 5 with the discussion of Fig. 6.

4 RESULTS

In this section, we present our main results. We first demonstrate in § 4.1 that our age matching model reproduces our new SDSS measurements of the projected galaxy 2PCF and galaxy-galaxy lensing as a function of stellar mass, and divided into quenched and star-forming populations. We then focus squarely on results pertinent to quenched and star-forming properties of satellite galaxies as measured from the $M_*^{9.8}$ SDSS group catalog. Specifically, in § 4.2 we compare our model prediction for the radial distribution of quenched and star-forming satellite galaxies within and around halos corresponding to group-, rich group- and cluster-size halos. We then examine the radial dependence of the quenched fraction of satellite galaxies in such regimes.

4.1 Galaxy Clustering and Galaxy-Galaxy Lensing

4.1.1 Clustering

We now investigate the success of age matching at predicting SFR-dependent clustering. Turning to the top row of Fig. 2, red and blue solid curves are our model predictions for the quenched and star-forming galaxy samples, respectively. Errors on the model $w_{\rm p}(r_{\rm p})$ predictions are estimated by jackknifing the octants of the simulation box. Red and blue filled circles are new measurements from SDSS (see Tables A1 & A2). Errors on the measurements are computed from jackknife resampling of 50 equal-area regions on the sky. A detailed description for how we calculate the clustering in the data and in the simulation can be found in § 2.2 and § 5.1 of Paper II, respectively. Our age matching predictions for the SFR-dependent clustering are in excellent agreement with the data at each stellar mass threshold sample and all projected separations. However, as seen in the top, center panel of Fig. 2 of Paper II, there is a slight under-prediction from abundance matching on small scales ($r_{\rm p} \lesssim 1h^{-1}{\rm Mpc}$) for the $\log_{10}(M_*) > 10.2$ threshold sample. This discrepancy naturally propagates through to both the quenched and star-forming age matching predictions (top, center panel), where the clustering amplitude on small scales is suppressed with respect to the data. However, the *relative* quenched and star-forming split of the model agrees well with that of the data.

4.1.2 Lensing

In addition to clustering, we also test our model against new SDSS measurements of the SFR-dependent galaxy-galaxy lensing signal, $\Delta\Sigma$, which are provided in Tables 3 & 4. In Paper II we describe how we calculate $\Delta\Sigma$ both in the data (§ 2.4) and in the simulation (§ 5.2). As was shown in Fig. 2 of Paper II, we accurately predict $\Delta\Sigma$ first at the abundance matching level, though it should be noted that the amplitude of the abundance matching prediction for each stellar mass threshold is slightly boosted relative to the data. Thus we expect the age matching, SFR-dependent $\Delta\Sigma$ amplitudes to be boosted for each sample as well. This is indeed the case as seen in the bottom row of Fig. 2.

SDSS data points for quenched and star-forming samples are represented as red and blue filled circles, respectively, while red and blue solid curves are the model predictions according to age matching. Errors on the $\Delta\Sigma$ model predictions are computed via 27 jackknife regions over the Bolshoi simulation volume. Errors on the SDSS lensing signal are derived by dividing the survey area into 200 bootstrap subregions and generating 500 bootstrap-resampled datasets. In light of the slight over-prediction of the model at the abundance matching level, the *relative* separation in $\Delta\Sigma$ between quenched and star-forming samples is predicted reasonably well for each stellar mass threshold, with the exception of the star forming samples on the very smallest scales.
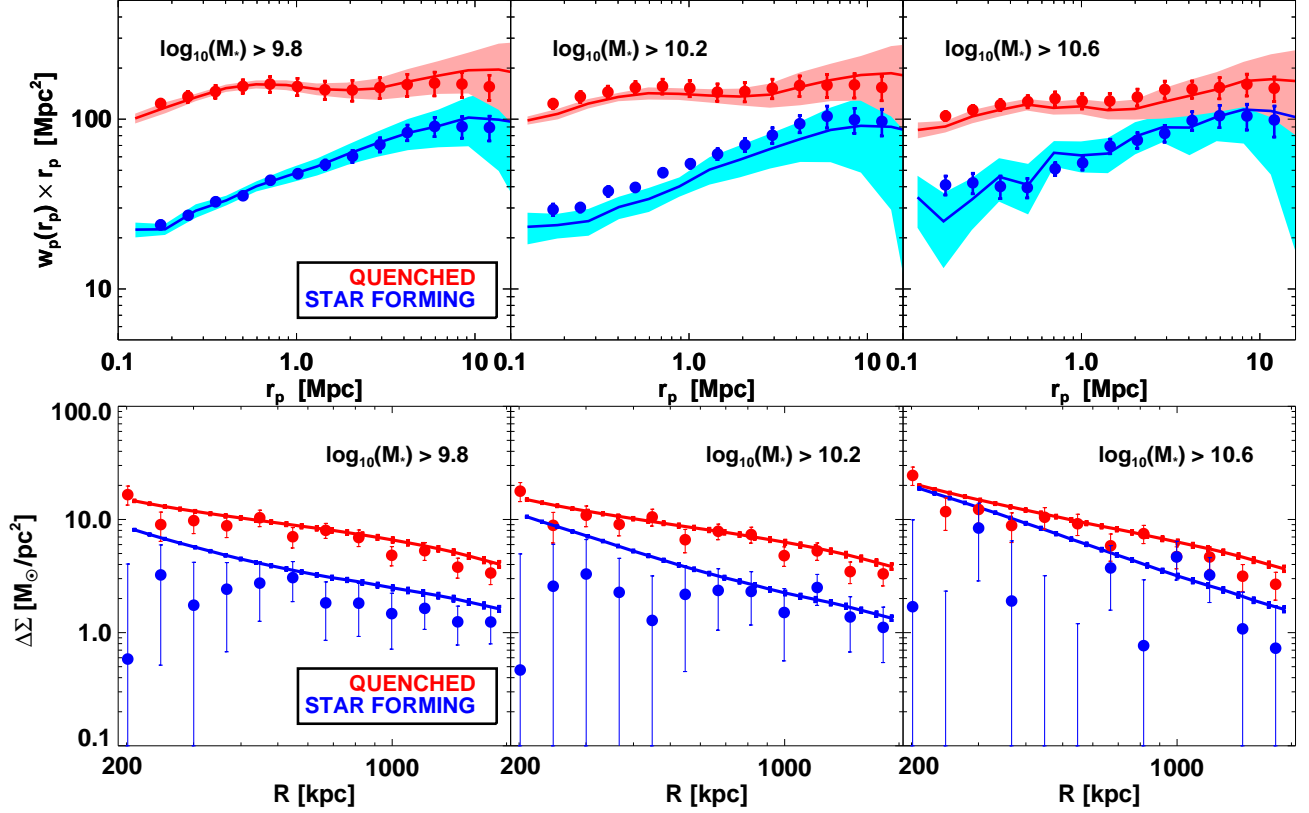
Figure 2. SFR-dependent clustering and galaxy-galaxy lensing as a function of stellar mass as predicted by our age matching model versus new SDSS measurements. **Top Row:** The projected correlation function (multiplied by r_p) predicted by our model split into quenched and star-forming mock galaxy samples is shown with red and blue solid curves, respectively. Solid bands in each panel show the error in our model prediction estimated by jackknifing the octants of the simulation box. Red (blue) points show our measurements of quenched (star-forming) SDSS galaxies (provided in Tables A1 & A2). Errors on the measurements are computed from jackknife resampling of 50 equal-area regions on the sky. **Bottom Row:** Excess surface density $\Delta\Sigma$ as a function of stellar mass and SFR as predicted by our age matching model (red and blue solid curves solid curves) in comparison to new SDSS measurements. Our new SDSS $\Delta\Sigma$ measurements are provided in Tables 3 & 4. Errors on the SDSS lensing signal are derived by dividing the survey area into 200 bootstrap subregions and generating 500 bootstrap-resampled datasets, while the age matching errors are computed via 27 jackknife regions over the simulation volume.

4.2 Star-Forming and Quenched Satellite Galaxies within Galaxy Groups, Rich Groups, and Clusters

We now focus on results pertaining specifically to satellite galaxies. By employing the same galaxy group finder to distinguish between central and satellite galaxies in both our mock catalog and the SDSS sample (see § 2 for details of the galaxy group finder we employ), we investigate the radial distribution of quenched and star-forming galaxies within group-, rich group- and cluster- size halos and their surrounding larger scale environment. We also study the radial dependence of the satellite galaxy quenched fraction, and test whether or not there is variation in the *slope* of the profile for these three regimes.

4.2.1 Radial Profiles of Star-Forming and Quenched Satellites

In our study of the radial profiles of satellites, we consider three standard regimes: groups, rich groups, and clusters, which we define as having host halo masses of $10^{12.5-13.25}, 10^{13.25-14}$, and $10^{14-15}h^{-1}M_\odot$, respectively. Host halo masses are assigned to groups in the traditional abundance matching manner, namely by matching the number density of Bolshoi *host* halos rank-ordered by M_vir to the number density of the groups rank-ordered by total stellar mass in the group. This procedure is done separately for the SDSS and mock catalogs, for consistency.

For each satellite in both the age matching mock and SDSS data, we measure r_p, the projected separation of the satellite from the group's central galaxy. For each group, we define R_group to be the rms group size. An alternative choice for group size would be the virial radius pre-
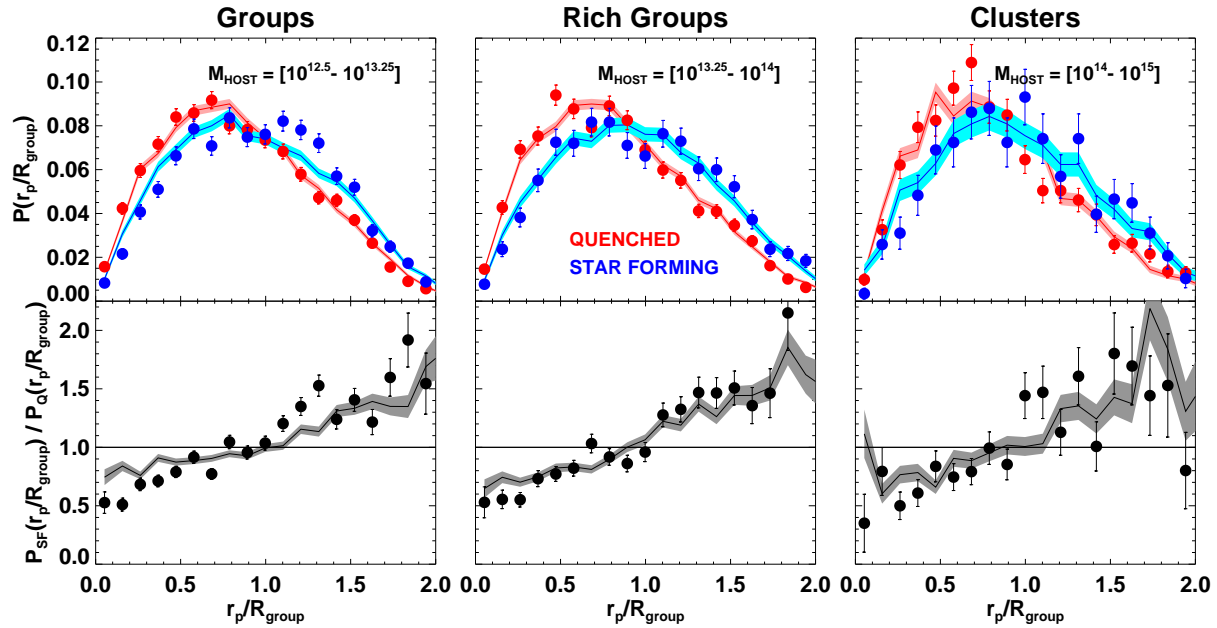
Figure 3. PDFs of the radial distribution of quenched ($P_Q(r_p/R_{group})$) and star forming ($P_{SF}(r_p/R_{group})$) galaxies within and around groups, rich groups, and clusters as measured in our galaxy group catalog. **Top Row:** Age matching predictions are shown as red and blue curves, respectively, versus the profiles measured in SDSS (red and blue filled circles). Three environmental regimes are considered corresponding to groups, rich groups, and clusters, which we define as having host halo masses of $10^{12.5-13.25}$, $10^{13.25-14}$, and $10^{14-15} h^{-1} M_\odot$, respectively. The radial separation on the x-axis, r_p/R_{group}, is defined as the projected separation, r_p, divided by the rms group size, R_{group} ($R_{group} \simeq 450 h^{-1}$kpc for groups, $\simeq 650 h^{-1}$kpc for rich groups, and $\simeq 1 h^{-1}$Mpc for clusters). In each host halo mass regime, quenched galaxies are more centrally concentrated then their star-forming counter parts. **Bottom Row:** We divide the star-forming population PDF by that of the quenched population of the top panels to highlight differences between the quenched and star-forming radial profiles. Results for the mock are shown as black solid lines with gray error bands, and filled black circles are for SDSS. Poisson errorbars are shown in all panels.
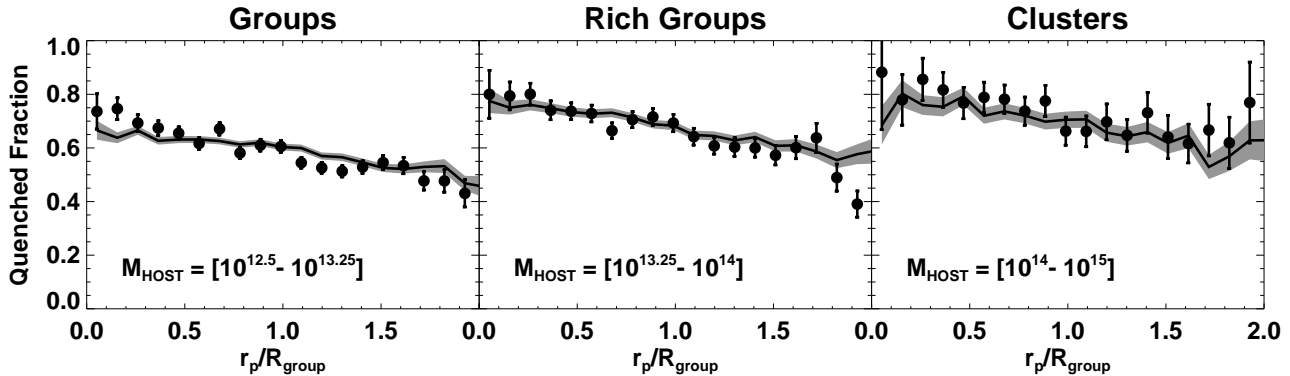

Figure 4. The overall quenched fraction of satellite galaxies versus projected distance from the central galaxy within and around group-, rich group-, and cluster-mass halos. The model prediction is striking: agreement with the SDSS data spans scales deep within host halos and extending out to radial separations well beyond the group radius for all three environments.

sumed to be associated with the group's halo, defined by $M_{vir} = (4\pi/3)R_{vir}^3 \Delta_{vir}\rho_m$, where ρ_m is the cosmic mean matter density, and $\Delta_{vir} \simeq 360$. However, R_{vir} and rms group size are in tight correspondence, with a scatter of $\sim 20\%$. We find that $R_{group} \simeq 450 h^{-1}$kpc, $650 h^{-1}$kpc, and $1 h^{-1}$Mpc for the group, rich group and cluster regimes, respectively.

Using these measurements, in the top row of Fig. 3 we show the PDFs of the radial distribution of quenched ($P_Q(r_p/R_{group})$) and star-forming galaxies ($P_{SF}(r_p/R_{group})$). Model predictions appear as red and blue curves, respectively, SDSS measurements appear as red and blue filled circles. Poisson error bars are shown in all panels.

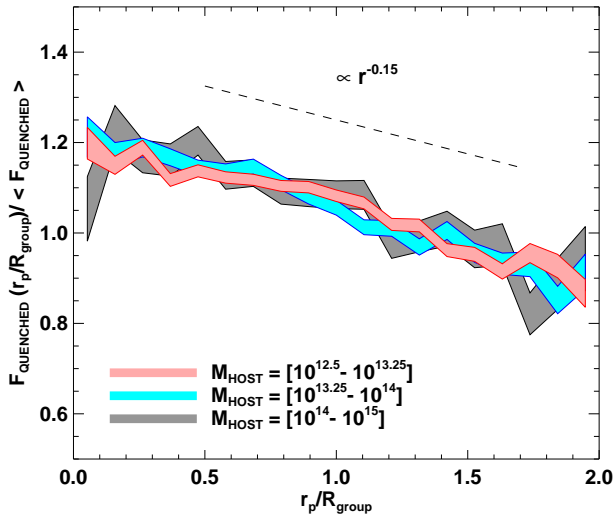First note that in each panel it is clear that quenched

Figure 5. The (lack of) environmental dependence of satellite quenching gradients. The model prediction in each panel of Fig. 4 is normalized by the *overall* mean satellite quenched fraction in each environment, so that on the y-axis of this figure we plot $F_{\rm QUENCHED}(r_{\rm p}/R_{\rm group})/\langle F_{\rm QUENCHED}\rangle$. What emerges is an $\sim r^{-0.15}$ slope, *independent of environment.*

galaxies are more centrally concentrated than their star-forming counterparts. There are in fact a larger *total* number of quenched than star-forming satellites at all scales, but here the $P_{\rm SF}(r_{\rm p}/R_{\rm group})$ and $P_{\rm Q}(r_{\rm p}/R_{\rm group})$ are separately unit-normalized in each host mass range, thus highlighting the level of accuracy of the age matching model with respect to the data. In the bottom row of Fig. 3 we divide $P_{\rm SF}(r_{\rm p}/R_{\rm group})$ by $P_{\rm Q}(r_{\rm p}/R_{\rm group})$ to highlight differences between the quenched and star-forming radial profiles. Results for SDSS are shown as filled black circles and black solid lines with gray error bands for the mock. Poisson errorbars are shown in all panels. Other than a slight discrepancy at very small projected separations for the galaxy group halo mass scale, there is excellent agreement between our model and these measurements for all three host mass regimes, and at all projected separations.

4.2.2   The Radial Dependence of the Satellite Galaxy Quenched Fraction

Figure 4 shows the overall quenched fraction as a function of $r_{\rm p}/R_{\rm group}$. In each bin of $r_{\rm p}/R_{\rm group}$, we compute the fraction of satellites found in that bin that are quenched, $F_{\rm QUENCHED}(r_{\rm p}/R_{\rm group})$. Again, the result is compelling: the age matching prediction is in agreement with the data on scales deep within the host halo of the group, and also extending out to scales well beyond the group radii. The overall amplitude of the radial quenched fraction increases when going from the group to cluster regime, as has been seen in other studies (e.g., Wetzel et al. 2013). Additionally, one can notice by eye that there is an apparent lack of $M_{\rm host}-$dependence of the *slope* of the profiles. To investigate this more closely, we separately normalize the radial quenched fractions for satellites in each host halo mass range (i.e., each panel of Fig. 4) by the overall

mean quenched fraction of satellites in groups of that mass, given as $F_{\rm QUENCHED}(r_{\rm p}/R_{\rm group})/\langle F_{\rm QUENCHED}\rangle$ on the y-axis of Fig. 5. The result is an $\sim r^{-0.15}$ slope for the radial quenched fraction of satellite galaxies, *independent of environment.*

As emphasized in Papers I & II, our age matching model has required no parameter fitting to achieve the agreement between the predicted and measured SFR-dependent galaxy statistics. There is good agreement between our model and SDSS measurements for the predicted clustering, lensing and satellite-specific spatial distributions within halos, despite the fact that the SFR-halo assignment in age matching has *no explicit dependence on halo position or post-accretion orbital history.* Thus, in our mock the SFR-dependent spatial distributions of both central and satellite galaxies simply emerges as a result of the galaxy-halo co-evolution ansatz.

5   DISCUSSION & INTERPRETATION

5.1   Simplifying the Galaxy Evolution Picture with Age Matching

The primary result of this paper is that the simple age matching model, in which galaxies and halos co-evolve, such that quenched galaxies reside in old halos, is able to predict a wide variety of observed SDSS galaxy statistics for quenched and star-forming galaxies. In our model, there are (1) no fine tuning or updates to the age matching model that proved successful at reproducing color-based SDSS measurements, (2) no distinction between central and satellite galaxies when assigning SFRs, and (3) no explicit modeling of post-accretion processes that are believed to stifle the star formation in satellite galaxies (e.g., strangulation, ram pressure stripping, etc.).

Let us consider these points in turn. As discussed in § 1, the color of a galaxy is known to be strongly correlated with star formation activity. For a variety of reasons, though, the correspondence is not perfect. For instance, active galaxies can often be classified as red due to the presence of dust (Maller et al. 2009; Masters et al. 2010). Color correlates with long term mass accretion history in age matching because of the timescale ($\sim$ Gyr) to evolve from the blue to red sequence. On the other hand, the timescales relevant to, for example, Hα indicators of SFR are significantly shorter than timescales impacting color (e.g., $\sim 10-100$Myr for the lifetime of O and B stars). Therefore, it is plausible that employing present day SFR in the age matching model may not exhibit the same level of success as a model based on $g-r$ color.

We have shown that this is not the case: the SFR predictions of our age matching implementation of CAM are equally successful as the color-based predictions from Papers I & II. Certainly the relatively tight scatter between $g-r$ and sSFR is partly responsible for this dual success. In a follow-up paper to the present work (Watson, Skibba & Hearin 2014, in prep), we will show that the shortcomings of using broadband color as a proxy for present day star formation activity have virtually no manifestation on the two-point function. This surprising result, interesting in its own right, provides further insight into the reason

that our model is able predict both $g - r$ color and SFR without modification. The explanation for this is simple: a star-forming galaxy appears red when our line of sight to the galaxy lies in the plane of its disk; for a *pair* of galaxies separated by $r \gtrsim 100$kpc, the probability of this occurrence is essentially independent due to the very weak correlation between galaxy alignments (Zhang et al. 2013).

Point (2) highlights the simplicity of age matching, as well as what drives the satellite quenching predictions of the model. Consider the implications of the left panel of Fig. 6. We use our mock catalog to show the average formation epoch of centrals (mock galaxies residing in host halos) in comparison to satellites (subhalos). As in Papers I & II, we use the Wechsler et al. (2002) concentration-based definition for the formation epoch of a halo. In age matching, despite there being no distinction between central and satellite galaxies when assigning a SFR, satellite galaxies are more quenched than their central galaxy counterparts at fixed stellar mass simply because subhalos form earlier than host halos.

The empirical justification for this cornerstone of age matching is illustrated in the right panel of Fig. 6, where we show the difference in the mean SFR of satellite and central galaxies in bins of fixed stellar mass. For this figure, we now use the group-finder to identify centrals and satellites, permitting a direct comparison to observational data. SDSS measurements are shown as black, filled circles and our age matching model prediction is shown as the solid black line with a gray error band (all errors are Poisson). At fixed stellar mass, satellites are more quenched than centrals in both the data and the model, and the observed quenching difference is quantitatively consistent with the difference implied by the relative formation times of host halos and subhalos.

This observation is closely connected to point (3). Age matching does not require any explicit modeling of post-infall effects on satellite galaxy quenching. The virial radius R_{vir} of host halos only enters into our model through the definition of z_{acc}, the epoch when a halo accretes onto a larger halo, thus becoming a subhalo. However, recall that in age matching, SFR is determined by z_{starve}, the redshift in a (sub)halo's MAH when it is deemed to be starved of the cold gas supply needed to continue fueling star formation. Formally, $z_{\mathrm{starve}} \equiv \mathrm{Max}\left\{z_{\mathrm{acc}}, z_{\mathrm{char}}, z_{\mathrm{form}}\right\}$, and as we showed in Paper II, the epoch z_{acc} has an essentially negligible impact on z_{starve} at all stellar masses, a result which also holds true in the present work. *Thus in our model, R_{vir} does not mark a special transition region in the evolution of a satellite,* and yet we accurately predict the radial profiles of quenched and star-forming galaxies both inside and well beyond the group radius, as well as the so-called "excess quenched fraction" of satellites (right panel of Fig. 6).

This qualitatively distinguishes age matching from conventional semi-analytic and empirical models of satellite quenching. We note, however, that the lack of explicit appearance of R_{vir} in our model does *not* imply that post-accretion processes are necessarily irrelevant to satellite quenching, since there is a significant correlation between the time a subhalo accretes onto a larger halo and the time the subhalo formed (see Fig. 6 of Paper II), rather that the overallin fluence of post-accretion physics has been overstated in the literature. Nonetheless, we will show in a pair of companion papers to this one that recent observations

of SFR trends in the low-redshift universe *do* favor a scenario in which quenching is impacted by physical processes that operate on scales far larger than R_{vir}, *even for central galaxies*, as discussed in the following section.

5.2   Discriminating between Competing Quenching Models

As discussed in detail in Zentner, Hearin & van den Bosch (2014), the success of age matching has exposed fundamental degeneracies in traditional approaches to galaxy-halo modeling such as the Halo Occupation Distribution (HOD, e.g., Seljak 2000; Cooray & Sheth 2002; Berlind & Weinberg 2002; Berlind et al. 2003; Zheng et al. 2005; Skibba & Sheth 2009a; Watson et al. 2010, 2012) and Conditional Luminosity Function (CLF, e.g., Yang et al. 2003; van den Bosch et al. 2013). While it is true that age matching is based on V_{max} to set the stellar mass or luminosity content of halos, the assignment of the additional galaxy properties of color or SFR is based on halo assembly history. Conversely, HOD modeling beyond just stellar mass- or luminosity - dependent clustering, i.e. the color or SFR dependence (e.g., Zehavi et al. 2005, 2011; Skibba & Sheth 2009b; Tinker et al. 2013; Guo et al. 2014b), is still exclusively governed by M_{vir} and no other halo property. And yet, both classes of models give very good descriptions of a wide variety of measurements of the galaxy distribution.

These considerations apply equally well to degeneracies with other common models of galaxy evolution. Indeed, both HODs and CLFs enjoy comparable levels of qualitative successes in reproducing observed statistics such as those presented in this work and the previous age matching papers. There is thus some legitimate cause for concern that conventional statistics describing the galaxy distribution are inadequate to conclusively discriminate between competing models. One particularly interesting measurement is that of *galactic conformity*, a feature in the galaxy distribution first discovered by Weinmann et al. (2006). In their analysis of an SDSS galaxy group catalog, Weinmann et al. (2006) showed that in group systems of the same halo mass, satellites in groups with a red central tend to be redder than satellites in groups with a blue central. In another recently reported detection of conformity, Kauffmann et al. (2013) showed that in an SDSS sample of central galaxies of the same stellar mass, the environment surrounding quenched central galaxies exhibits, on average, an attenuated SFR relative to the environment around star-forming centrals, a correlation that persists out to scales of $R \sim 5$Mpc, far outside the virial radius of the host halo of the centrals.

As we show in a recent paper (Hearin, Watson & van den Bosch 2014), these closely related signals are formally distinct in the following sense: the Weinmann et al. (2006) notion of conformity pertains to SFR correlations between central and satellite galaxies in the same dark matter halo, while the larger scale Kauffmann et al. (2013) signal pertains to SFR correlations in distinct halos. We contend that no galaxy evolution model in which central galaxy SFR is exclusively determined by halo mass M_{vir} (and subsequently virial radius R_{vir}) can account for either signal, as there would be
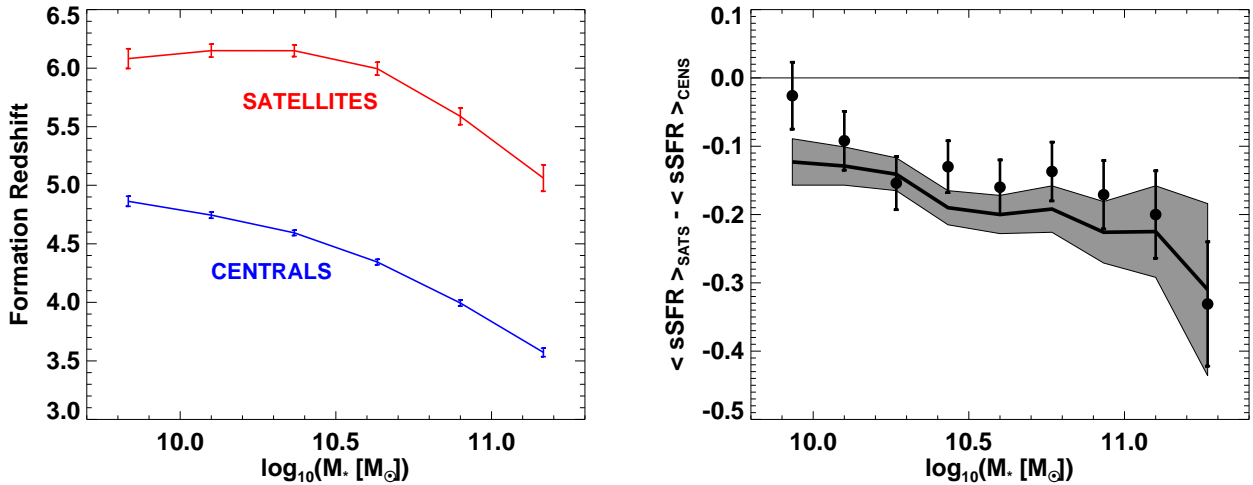
Figure 6. Left Panel: Formation epoch of central (blue curve) and satellite (red curve) galaxies as a function of stellar mass. Satellites in our model are more quenched than central galaxies of the same stellar mass simply because subhalos form earlier than host halos. This fact about structure formation in CDM is what drives satellite quenching in the age matching model. **Right Panel:** The difference between the average SFR of satellite and central galaxies as a function of stellar mass for SDSS (filled, black circles) and our age matching prediction (black solid line). Poisson errors are shown for both data and the model. At fixed stellar mass satellites have lower SFRs than their central galaxy counterparts.

no mechanism by which such correlations could arise. However, in age matching, galaxies in the same environment evolve from collapsed peaks of the same region of the initial cosmic density field. Thus the known correlation between the formation times of nearby halos (e.g., Sheth & Tormen 2004; Wechsler et al. 2006) naturally gives rise to correlated stellar mass assembly histories of nearby galaxies. In Hearin, Watson & van den Bosch (2014) we demonstrate that age matching predicts galactic conformity of both the Weinmann et al. (2006) and Kauffmann et al. (2013) varieties, with no modifications to the model presented in this work. Since it was shown in Kauffmann et al. (2013) that the Guo et al. (2011) semi-analytic model (SAM) does not predict conformity, this signal appears to be a promising testbed for the further development of galaxy evolution models.[5]

5.3   Future Directions

This trilogy of age matching papers has revealed that there is a surprisingly simple relationship between the star formation activity of a galaxy and the assembly history of its dark matter halo. However, there are two clear paths to challenging the age matching picture of galaxy and halo co-evolution. First, our model has only been tested for central and satellite galaxies of $\log_{10}(M_*) > 9.8$. However, using observations of classical dwarf galaxies in SDSS, Geha et al. (2012) discovered that there is an apparent stellar mass

---

[5] For example, the "pre-heating" of gas in the inter-galactic medium implemented in the SAM recently introduced in Lu et al. (2014) is a promising mechanism by which conformity may arise, as discussed in Kauffmann et al. (2013).

threshold of $\log_{10}(M_*) = 9.0$, below which quenched galaxies do not exist in the field. In a recent study of this SDSS dwarf sample, Wheeler et al. (2014) demonstrated that the so-called "quenching timescale" after a satellite first crosses the virial radius R_{vir} of its host halo must be implausibly long ($\gtrsim 9\mathrm{Gyr}$) to produce the trends reported in Geha et al. (2012). These results are intriguingly in keeping with the notion supported by age matching that the role of R_{vir} has been over-estimated in the literature. In future work, we aim to apply the CAM modeling technique to dwarf galaxy samples to investigate whether the SFR trends exhibited by galaxies in this mass range are also reflected in a simple way by the evolutionary history of dark matter halos.

The second consideration will be confronting age matching with observations at higher redshift. We will soon take this crucial next step thanks to high-completeness data sets such as PRIMUS (Coil et al. 2011), GAMA (Driver et al. 2011) and VIPERS (Guzzo et al. 2013).

Ultimately, the power of this class of semi-empirical models is their ability to be used as "training sets" to help inform more complicated models of galaxy formation that include prescriptions for physical processes *a priori*. Specifically, SAMs and hydrodynamic simulations can draw insight from age matching in order to improve their input physical recipes.

6   SUMMARY

In this paper we have explored the hypothesis that the star formation rates (SFRs) of galaxies can be determined via the ansatz that galaxies co-evolve with their dark matter halos. Specifically, we have studied the age matching formalism introduced in Hearin & Watson (2013), whose central tenet is that red/quenched galaxies reside in old halos,

and conversely for blue/star-forming galaxies. This simple formalism has been proven to be remarkably powerful, yielding accurate predictions of SDSS color-dependent clustering and galaxy-galaxy lensing, as well as a variety of galaxy group-based statistics. In this work have confronted our age matching formalism with SFR-dependent, low-redshift galaxy statistics. Specifically, we have found the following principal results.

• We present new measurements of SDSS clustering and galaxy-galaxy lensing as a function of stellar mass, split into distinct quenched and star-forming populations. The same age matching prescription introduced in Paper I and extended in Paper II adapts seamlessly to accurately predict these SFR-dependent observations, *without necessitating updates to the model or fine-tuning/fitting of parameters.*
• Age matching predictions are in excellent agreement with the observed radial distribution of star-forming and quenched satellite galaxies within and around galaxy group, rich group, and cluster environments, a success that extends significantly beyond the group radius.
• We demonstrate the lack of halo mass-dependence in the slope of the radial quenched fraction of satellites, finding an $\sim r^{-.15}$ gradient *independent of environment.*
• We make our mock galaxy catalog publicly available at `http://logrus.uchicago.edu/~aphearin`.

These findings provide compelling evidence for the co-evolution of halos and galaxies, and are highly suggestive of the conclusion that the existing literature has overestimated the role of post-accretion processes on attenuating star formation in satellite galaxies. We consider the myriad successes of our model to indicate that there does indeed exist a simple relation between cosmic star formation history of galaxies and the dark side of the universe.

REFERENCES

Abazajian K. N., Adelman-McCarthy J. K., Agüeros M. A., Allam S. S., Allende Prieto C., An D., Anderson K. S. J., Anderson S. F., Annis J., Bahcall N. A., et al. 2009, ApJS , 182, 543

Baldry I. K., Glazebrook K., Brinkmann J., Ivezić Ž., Lupton R. H., Nichol R. C., Szalay A. S., 2004, ApJ , 600, 681

Balogh M. L., Morris S. L., Yee H. K. C., Carlberg R. G., Ellingson E., 1999, ApJ , 527, 54

Behroozi P. S., et al., 2013a, ApJ , 763, 18

Behroozi P. S., et al., 2013b, ApJ , 762, 109

Behroozi P. S., Wechsler R. H., Conroy C., 2013a, ApJL , 762, L31

Behroozi P. S., Wechsler R. H., Conroy C., 2013b, ApJ , 770, 57

Behroozi P. S., Wechsler R. H., Lu Y., Hahn O., Busha M. T., Klypin A., Primack J. R., 2013, ArXiv:1310.2239

Bell E. F., et al., 2004, ApJ , 608, 752

Berlind A. A., et al., 2003, ApJ , 593, 1

Berlind A. A., et al., 2006, ApJS , 167, 1

Berlind A. A., Weinberg D. H., 2002, ApJ , 575, 587

Bernardi M., Meert A., Sheth R. K., Vikram V., Huertas-Company M., Mei S., Shankar F., 2013, MNRAS , 436, 697

Berrier J. C., Bullock J. S., Barton E. J., Guenther H. D., Zentner A. R., Wechsler R. H., 2006, ApJ , 652, 56

Berrier J. C., Cooke J., 2012, MNRAS , 426, 1647

Blanton M. R., Eisenstein D., Hogg D. W., Schlegel D. J., Brinkmann J., 2005, ApJ , 629, 143

Blanton M. R., et al., 2003, ApJ , 594, 186

Brinchmann J., Charlot S., White S. D. M., Tremonti C., Kauffmann G., Heckman T., Brinkmann J., 2004, MNRAS , 351, 1151

Carollo C. M., et al., 2013, ApJ , 776, 71

Coil A. L., et al., 2011, ApJ , 741, 8

Conroy C., Wechsler R. H., 2009, ApJ , 696, 620

Conroy C., Wechsler R. H., Kravtsov A. V., 2006, ApJ , 647, 201

Cooper M. C., et al., 2006, MNRAS , 370, 198

Cooper M. C., et al., 2012, MNRAS , 419, 3018

Cooray A., Sheth R., 2002, Phys. Rep. , 372, 1

Dekel A., Birnboim Y., 2006, MNRAS , 368, 2

Driver S. P., et al., 2011, MNRAS , 413, 971

Geha M., Blanton M. R., Yan R., Tinker J. L., 2012, ApJ , 757, 85

Gunn J. E., Gott III J. R., 1972, ApJ , 176, 1

Guo H., et al., 2014a, ArXiv:1401.3009

Guo H., et al., 2014b, ArXiv: 1401.3009

Guo Q., Cole S., Eke V., Frenk C., 2011, MNRAS , 417, 370

Guo Q., White S., Li C., Boylan-Kolchin M., 2010, MNRAS , 404, 1111

Guzzo L., et al., 2013, ArXiv:1303.2623

Hearin A. P., et al., 2014, MNRAS , 444, 729

Hearin A. P., Watson D. F., 2013, MNRAS , 435, 1313

Hearin A. P., Watson D. F., van den Bosch F. C., 2014, ArXiv:1404.6524

Hearin A. P., Zentner A. R., Berlind A. A., Newman J. A., 2013, MNRAS , 433, 659

Kauffmann G., et al., 2003, MNRAS , 341, 33

Kauffmann G., Li C., Zhang W., Weinmann S., 2013, MN-RAS , 430, 1447

Klypin A. A., Trujillo-Gomez S., Primack J., 2011, ApJ , 740, 102

Kravtsov A., Vikhlinin A., Meshscheryakov A., 2014, ArXiv: 1401.7329

Kravtsov A. V., 2013, ApJL , 764, L31

Kravtsov A. V., Berlind A. A., Wechsler R. H., Klypin A. A., Gottlöber S., Allgood B., Primack J. R., 2004, ApJ , 609, 35

Larson R. B., Tinsley B. M., Caldwell C. N., 1980, ApJ , 237, 692

Leitner S. N., 2012, ApJ , 745, 149

Li C., Kauffmann G., Jing Y. P., White S. D. M., Börner G., Cheng F. Z., 2006, MNRAS , 368, 21

Lu Z., Mo H. J., Lu Y., Katz N., Weinberg M. D., van den Bosch F. C., Yang X., 2014, MNRAS

Maller A. H., Berlind A. A., Blanton M. R., Hogg D. W., 2009, ApJ , 691, 394

Martizzi D., Teyssier R., Moore B., 2012, MNRAS , 420, 2859

Masters K. L., et al., 2010, MNRAS , 404, 792

Moore B., Lake G., Katz N., 1998, ApJ , 495, 139

Mostek N., Coil A. L., Cooper M., Davis M., Newman J. A., Weiner B. J., 2013, ApJ , 767, 89

Moster B. P., Naab T., White S. D. M., 2013, MNRAS , 428, 3121

Norberg P., et al., 2002, MNRAS , 332, 827

Peng Y.-j., et al., 2010, ApJ , 721, 193

Peng Y.-j., Lilly S. J., Renzini A., Carollo M., 2012, ApJ , 757, 4

Purcell C. W., Bullock J. S., Zentner A. R., 2007, ApJ , 666, 20

Reddick R. M., Wechsler R. H., Tinker J. L., Behroozi P. S., 2013, ApJ , 771, 30

Riebe K., Partl A. M., Enke H., Forero-Romero J., Gottlöber S., Klypin A., Lemson G., Prada F., Primack J. R., Steinmetz M., Turchaninov V., 2013, Astronomische Nachrichten, 334, 691

Rodríguez-Puebla A., Drory N., Avila-Reese V., 2012, ApJ , 756, 2

Salim S., et al., 2007, ApJS , 173, 267

Seljak U., 2000, MNRAS , 318, 203

Shankar F., Lapi A., Salucci P., De Zotti G., Danese L., 2006, ApJ , 643, 14

Sheth R. K., Tormen G., 2004, MNRAS , 350, 1385

Skibba R., Sheth R. K., Connolly A. J., Scranton R., 2006, MNRAS , 369, 68

Skibba R. A., et al., 2013, MNRAS , 429, 458

Skibba R. A., Sheth R. K., 2009a, MNRAS , 392, 1080

Skibba R. A., Sheth R. K., 2009b, MNRAS , 392, 1080

Stein W. A., Soifer B. T., 1983, ARAA , 21, 177

Tal T., et al., 2014, ArXiv e-prints

Tasitsiomi A., Kravtsov A. V., Wechsler R. H., Primack J. R., 2004, ApJ , 614, 533

Teyssier R., Moore B., Martizzi D., Dubois Y., Mayer L., 2011, MNRAS , 414, 195

Tinker J. L., et al., 2013, ApJ , 778, 93

Trujillo-Gomez S., Klypin A., Primack J., Romanowsky A. J., 2011, ApJ , 742, 16

Vale A., Ostriker J. P., 2004, MNRAS , 353, 189

Vale A., Ostriker J. P., 2006, MNRAS , 371, 1173

van den Bosch F. C., et al., 2008, MNRAS , 387, 79

van den Bosch F. C., More S., Cacciato M., Mo H., Yang X., 2013, MNRAS , 430, 725

Wang L., Farrah D., Oliver S. J., Amblard A., Bock J., Conley A., Cooray A., Halpern M., Heinis S., Ibar E., Ilbert O., Ivison R. J., Marsden G., Roseboom I. G., Rowan-Robinson M., Schulz B., Smith A. J., Viero M., Zemcov M., 2012, ArXiv: 1203.5828

Wang L., Jing Y. P., 2010, MNRAS , 402, 1796

Watson D. F., Berlind A. A., McBride C. K., Hogg D. W., Jiang T., 2012, ApJ , 749, 83

Watson D. F., Berlind A. A., McBride C. K., Masjedi M., 2010, ApJ , 709, 115

Watson D. F., Berlind A. A., Zentner A. R., 2012, ApJ , 754, 90

Watson D. F., Conroy C., 2013, ApJ , 772, 139

Wechsler R. H., Bullock J. S., Primack J. R., Kravtsov A. V., Dekel A., 2002, ApJ , 568, 52

Wechsler R. H., Zentner A. R., Bullock J. S., Kravtsov A. V., Allgood B., 2006, ApJ , 652, 71

Weinmann S. M., Kauffmann G., van den Bosch F. C., Pasquali A., McIntosh D. H., Mo H., Yang X., Guo Y., 2009, MNRAS , 394, 1213

Weinmann S. M., van den Bosch F. C., Yang X., Mo H. J., 2006, MNRAS , 366, 2

Wetzel A. R., Tinker J. L., Conroy C., 2012, MNRAS , 424, 232

Wetzel A. R., Tinker J. L., Conroy C., van den Bosch F. C., 2013, MNRAS , 432, 336

Wheeler C., Phillips J. I., Cooper M. C., Boylan-Kolchin M., Bullock J. S., 2014, ArXiv:1402.1498

Wyder T. K., et al., 2007, ApJS , 173, 293

Yang X., Mo H. J., van den Bosch F. C., 2003, MNRAS , 339, 1057

Yang X., Mo H. J., van den Bosch F. C., Zhang Y., Han J., 2012, ApJ , 752, 41

York D. G., et al., 2000, AJ , 120, 1579

Zehavi I., et al., 2002, ApJ , 571, 172

Zehavi I., et al., 2005, ApJ , 630, 1

Zehavi I., et al., 2011, ApJ , 736, 59

Zentner A. R., Hearin A. P., van den Bosch F. C., 2014, MNRAS , 443, 3044

Zhang Y., Yang X., Wang H., Wang L., Mo H. J., van den Bosch F. C., 2013, ApJ , 779, 160

Zheng Z., Berlind A. A., Weinberg D. H., Benson A. J., Baugh C. M., Cole S., Davé R., Frenk C. S., Katz N., Lacey C. G., 2005, ApJ , 633, 791

APPENDIX A: SDSS GALAXY CLUSTERING AND GALAXY-GALAXY LENSING MEASUREMENTS

Table A1. SDSS PROJECTED CORRELATION FUNCTION MEASUREMENTS: STAR-FORMING GALAXIES.
The first column is the mean radii of galaxies in each logarithmic bin in units of Mpc. Additional columns show the projected correlation function, $w_\mathrm{p}(r_\mathrm{p})$, for star forming ($\log_{10}(\mathrm{sSFR}) > -11$) galaxies for three stellar mass, volume-limited threshold samples: $\log_{10}(M_*) >$ [9.8, 10.2, 10.6]. Errors are computed from jackknife resampling of 50 equal-area regions on the sky, and the diagonal terms of the error covariance matrix are given in the parenthesis.

r_p	9.8	10.2	10.6
0.121	167.63 (9.52)	212.20 (15.74)	376.24 (68.50)
0.173	137.91 (7.47)	169.69 (12.99)	236.99 (30.19)
0.247	109.89 (5.66)	122.74 (7.31)	171.51 (23.77)
0.352	92.71 (4.97)	106.72 (7.02)	114.35 (17.39)
0.501	70.63 (3.61)	79.28 (4.59)	79.55 (10.41)
0.714	61.20 (3.19)	67.80 (3.71)	71.64 (6.13)
1.017	46.95 (2.62)	53.73 (3.19)	54.41 (4.99)
1.448	37.27 (2.40)	43.11 (3.20)	47.91 (4.73)
2.060	29.37 (2.38)	34.29 (3.03)	36.58 (3.86)
2.934	24.14 (2.29)	27.45 (2.89)	28.17 (3.15)
4.178	19.97 (2.11)	22.51 (2.60)	23.54 (2.99)
5.946	15.25 (1.98)	17.50 (2.57)	17.63 (2.64)
8.467	10.67 (1.55)	11.72 (1.97)	12.34 (2.14)
12.056	7.41 (1.23)	8.05 (1.44)	8.21 (1.70)
17.163	4.16 (1.06)	4.28 (1.20)	4.34 (1.53)

Table A2. SDSS PROJECTED CORRELATION FUNCTION MEASUREMENTS: QUENCHED GALAXIES. Same as Table A2, but for the quenched galaxy sample: $\log_{10}(\mathrm{sSFR}) < -11$.

r_p	9.8	10.2	10.6
0.121	937.41 (55.17)	952.28 (56.54)	906.32 (50.58)
0.173	714.72 (42.57)	713.58 (44.09)	603.32 (36.62)
0.247	552.16 (40.38)	551.71 (40.77)	460.28 (28.24)
0.352	414.42 (35.66)	411.74 (33.96)	346.20 (25.24)
0.501	312.35 (28.37)	306.81 (26.41)	254.14 (20.73)
0.714	226.84 (23.97)	220.18 (22.02)	186.01 (17.48)
1.017	154.15 (18.02)	150.92 (16.68)	127.03 (13.17)
1.448	103.35 (12.78)	100.13 (11.64)	88.78 (9.53)
2.060	72.28 (10.07)	70.81 (9.27)	65.63 (7.43)
2.934	52.52 (7.36)	51.86 (6.84)	51.03 (6.09)
4.178	38.36 (5.69)	37.86 (5.22)	36.04 (4.18)
5.946	27.48 (4.39)	26.73 (4.17)	25.88 (3.70)
8.467	19.03 (3.18)	18.83 (3.08)	18.99 (2.80)
12.056	12.90 (2.17)	12.78 (2.11)	12.64 (2.08)
17.163	7.73 (1.66)	7.53 (1.66)	7.29 (1.66)

Table A3. SDSS GALAXY-GALAXY LENSING MEASUREMENTS: STAR-FORMING GALAXIES. The first column is the mean radii of galaxies in each logarithmic bin, in units of kpc. Subsequent columns show the galaxy-galaxy lensing signal, $\Delta\Sigma$, in units of $M_\odot \mathrm{pc}^{-2}$ for the same three stellar mass, volume-limited threshold samples. Errors in the parenthesis are derived from dividing the survey area into 200 bootstrap subregions and generating 500 bootstrap-resampled data sets.

R	9.8	10.2	10.6
31.87	25.20 (20.58)	27.49 (26.79)	-25.63 (46.62)
38.93	24.35 (16.23)	33.66 (21.47)	76.67 (37.55)
47.54	53.35 (12.37)	58.77 (15.59)	79.43 (31.38)
58.07	25.61 (10.94)	31.28 (14.38)	28.00 (28.56)
70.93	22.93 (9.57)	26.64 (11.99)	18.30 (21.53)
86.63	11.06 (7.23)	7.53 (9.68)	28.00 (18.08)
105.81	17.59 (5.64)	11.42 (7.14)	26.59 (11.84)
129.24	1.95 (5.41)	-1.28 (7.41)	11.41 (11.80)
157.85	3.16 (4.01)	10.58 (5.29)	21.32 (9.11)
192.80	2.66 (3.00)	2.05 (3.89)	1.61 (7.33)
235.49	3.35 (2.85)	8.51 (3.69)	7.15 (6.87)
287.63	0.41 (2.42)	0.33 (3.15)	1.19 (5.76)
351.31	2.26 (1.90)	1.80 (2.42)	-2.55 (4.18)
429.09	1.22 (1.71)	2.31 (2.34)	5.88 (3.87)
524.09	1.69 (1.22)	1.59 (1.58)	1.33 (3.19)
640.13	1.92 (1.04)	0.90 (1.32)	-0.21 (2.44)
781.85	2.14 (0.83)	1.52 (1.21)	-1.26 (2.10)
954.96	1.28 (0.68)	1.65 (0.92)	2.61 (1.50)
1166.39	1.27 (0.63)	1.62 (0.80)	0.54 (1.51)
1424.63	1.03 (0.53)	1.05 (0.66)	3.27 (1.22)
1740.04	1.15 (0.40)	1.75 (0.53)	2.26 (0.96)
2125.29	0.87 (0.33)	0.96 (0.49)	0.76 (0.84)
2595.84	0.87 (0.31)	0.78 (0.40)	0.51 (0.70)
3170.56	0.52 (0.23)	0.65 (0.31)	0.49 (0.55)

Table A4. SDSS GALAXY-GALAXY LENSING MEASUREMENTS: QUENCHED GALAXIES. Same as Table 3, but for the quenched galaxy sample.

R	9.8	10.2	10.6
31.87	63.93 (20.39)	67.10 (21.61)	108.45 (29.36)
38.93	19.61 (19.42)	23.82 (20.14)	38.28 (24.27)
47.54	49.80 (14.42)	58.03 (15.50)	62.67 (19.85)
58.07	35.86 (10.89)	38.84 (11.68)	34.55 (14.83)
70.93	16.36 (9.28)	20.42 (9.48)	28.13 (13.60)
86.63	19.23 (7.35)	16.20 (7.49)	20.33 (10.20)
105.81	16.45 (6.09)	14.62 (6.42)	20.09 (8.52)
129.24	19.80 (5.42)	17.45 (5.33)	23.94 (6.82)
157.85	7.47 (4.47)	6.47 (4.44)	9.73 (5.47)
192.80	10.42 (4.11)	12.09 (4.23)	14.98 (5.39)
235.49	6.39 (3.07)	5.33 (3.20)	6.38 (3.99)
287.63	11.60 (2.22)	12.45 (2.38)	17.15 (3.17)
351.31	6.31 (1.83)	6.21 (1.87)	8.21 (2.61)
429.09	6.84 (1.59)	7.63 (1.58)	8.59 (2.10)
524.09	6.16 (1.31)	6.34 (1.32)	6.19 (1.82)
640.13	7.25 (1.20)	7.37 (1.25)	7.32 (1.58)
781.85	4.93 (1.01)	4.64 (1.08)	6.42 (1.37)
954.96	5.61 (0.85)	5.50 (0.87)	4.10 (1.11)
1166.39	4.84 (0.81)	5.15 (0.83)	5.25 (0.96)
1424.63	3.38 (0.65)	3.35 (0.66)	3.29 (0.72)
1740.04	3.70 (0.66)	3.69 (0.65)	3.26 (0.73)
2125.29	2.65 (0.53)	2.42 (0.52)	2.21 (0.59)
2595.84	2.35 (0.49)	2.31 (0.50)	1.87 (0.52)
3170.56	2.26 (0.42)	2.13 (0.42)	1.71 (0.39)